Int. J. Heat Mass Transfer. Vol. 33, No. 3, pp. 465–481, 1990
Printed in Great Britain

0017–9310/90 $3.00 + 0.00


# A sensitivity study of the effects of evaporation/condensation accommodation coefficients on transient heat pipe modeling

MICHAEL L. HALL
Los Alamos National Laboratory, Group N-6, MS K559, P.O. Box 1663, Los Alamos, NM 87545, U.S.A.

and

J. MICHAEL DOSTER
Nuclear Engineering Department, North Carolina State University, Box 7909, Raleigh, NC 27695, U.S.A.

(*Received* 12 *December* 1988 *and in final form* 6 *June* 1989)

**Abstract**—The dynamic behavior of liquid metal heat pipe models is strongly influenced by the choice of evaporation and condensation modeling techniques. Classic kinetic theory descriptions of the evaporation and condensation processes are often inadequate for real situations; empirical accommodation coefficients are commonly utilized to reflect nonideal mass transfer rates. The complex geometries and flow fields found in proposed heat pipe systems cause considerable deviation from the classical models. The THROHPUT code, which has been described in previous works, was developed to model transient liquid metal heat pipe behavior from frozen startup conditions to steady state full power operation. It is used here to evaluate the sensitivity of transient liquid metal heat pipe models to the choice of evaporation and condensation accommodation coefficients. Comparisons are made with experimental liquid metal heat pipe data. It is found that heat pipe behavior can be predicted with the proper choice of the accommodation coefficients. However, the common assumption of spatially constant accommodation coefficients is found to be a limiting factor in the model.

## 1. INTRODUCTION

A HEAT pipe is a closed heat transfer system, generally in the form of a simple cylindrical pipe sealed at both ends and partially filled with a working fluid. Heat from an external source is added at one end of the heat pipe, causing the working fluid to evaporate. The vapor expands into the heat pipe core and travels down a central adiabatic region (adiabatic only with respect to the surroundings) to the far end of the heat pipe where it condenses on the inner walls. The latent heat released in the condensation process is transferred through the walls of the heat pipe to the exterior surfaces and subsequently to the environment. The condensate is then 'pumped' back to the evaporator section through the capillary action of an embedded wick structure. A side view of this process is shown in Fig. 1. The net result of this cycle is the transfer of a large amount of heat, equal to the latent heat of the working fluid, all without the use of pumps, working parts of even gravitational forces. These characteristics make heat pipes particularly attractive to designers of space satellites.

Heat pipes can be constructed to operate with a variety of working fluids, the choice depending primarily on a match between the evaporation temperature and the desired operating temperature. Many of the recent designs of space satellites have employed heat pipes to form isothermal fins on a radiator panel assembly or to transfer heat from the reactor [1–6]. Both of these require high operating temperatures, such that a liquid metal, usually liquid lithium, is the working fluid of choice. However, the choice of lithium as a working fluid is not without problems. At ambient temperatures, lithium exists as a solid. Since the satellite will be launched in a cold state, the heat pipe should be able to begin operation with its lithium frozen. The ability of the heat pipe to self-prime is crucial to its usefulness. If operation is stopped during flight, the lithium will again solidify. A restart from this situation differs from the original startup in the distribution of the solid lithium. In this case, the solid will probably be concentrated in the condenser section, making startup even more difficult. Of additional concern is the reaction of the heat pipe

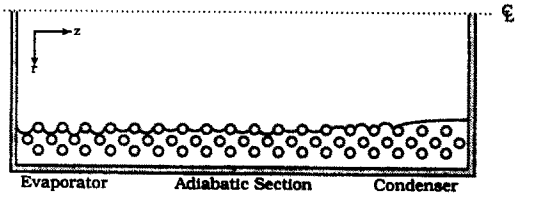


FIG. 1. Variation of the radius of curvature along the heat pipe.

## NOMENCLATURE

| | |
|---|---|
| $A$ | area [$m^2$] |
| $b$ | velocity ratio [dimensionless] |
| $c_p$ | specific heat [J $kg^{-1}$ $K^{-1}$] |
| $D$ | diffusion coefficient [$m^2$ $s^{-1}$] |
| $D^+$ | diffusion parameter defined in equation (21) [kg mol $kg^{-1}$] |
| $D_h$ | hydraulic diameter [m] |
| $\mathscr{F}$ | friction coefficient [kg $m^{-3}$ $s^{-1}$] |
| $g_z$ | $z$-component of the gravity vector [m $s^{-2}$] |
| $h$ | enthalpy [J $kg^{-1}$] |
| $\Delta h_{ls}$ | melting enthalpy difference, $h_l - h_s$ [J $kg^{-1}$] |
| $H$ | heat transfer coefficient [W $m^{-2}$ $K^{-1}$] |
| $j$ | diffusive flux [kg $m^{-2}$ $s^{-1}$] |
| $k$ | thermal conductivity [W $m^{-1}$ $K^{-1}$] |
| $L$ | axial length [m] |
| $m$ | molecular weight [kg $kg^{-1}$ $mol^{-1}$] |
| $\dot{m}$ | evaporation/condensation mass flux [kg $m^{-2}$ $s^{-1}$] |
| $P$ | pressure [Pa] |
| $\Delta P_{cap}$ | capillary pressure difference, $P_m - P_l$ [Pa] |
| $Q_{xy}$ | heat transfer rate from $x$ to $y$ [W $m^{-3}$] |
| $Q_{in}$ | external to wall heat transfer rate [W $m^{-3}$] |
| $Q_T$ | total heat throughput [W] |
| $r$ | radius [m] |
| $r_c$ | radius of curvature of the interphasic meniscus [m] |
| $r_i$ | inner radius of the heat pipe, liquid outer radius [m] |
| $r_o$ | outer radius of the heat pipe, wall outer radius [m] |
| $r_p$ | pore radius or minimum radius of curvature [m] |
| $R$ | gas constant [J $kg^{-1}$ $K^{-1}$] |
| $t$ | time [s] |
| $T$ | temperature [K] |
| $U$ | internal energy [J $kg^{-1}$] |
| V | volume [$m^3$] |
| $V$ | velocity [m $s^{-1}$] |
| $X$ | mass fraction [dimensionless] |
| $z$ | axial distance [m]. |

Greek symbols

| | |
|---|---|
| $\alpha$ | volume fraction [dimensionless] |
| $\beta$ | evaporation rate constant defined in equation (24) |
| $\Gamma_{xy}$ | mass transfer rate from $x$ to $y$ [kg $m^{-3}$ $s^{-1}$] |
| $\varepsilon_v$ | flow volume fraction in the wick [dimensionless] |
| $\varepsilon_s$ | surface fraction of the wick available for phasic interface [dimensionless] |
| $\mu$ | cosine of surface contact angle [dimensionless] |
| $\pi$ | ratio of the circumference to the diameter [dimensionless] |
| $\rho$ | density [kg $m^{-3}$] |
| $\sigma$ | liquid surface tension [N $m^{-1}$] |
| $\sigma_c$ | condensation accommodation coefficient [dimensionless] |
| $\sigma_e$ | evaporation accommodation coefficient [dimensionless]. |

Superscripts

| | |
|---|---|
| K | related to Knudsen diffusion |
| M | based on molecular fluxes or molecular average velocities |
| $n$ | time step |
| $X$ | related to a mass fraction |
| $\Gamma$ | related to interphase transfer |
| $\nu$ | normal (to the surface) value |
| $\rho$ | related to a density. |

Subscripts

| | |
|---|---|
| a | adiabatic section value |
| A, B | species in a binary mixture |
| amb | ambient value |
| b | bulk fluid value |
| c | condenser (or condensing) value |
| e | evaporator (or evaporating) value |
| eff | effective value |
| g | lithium gas value |
| i | wall inner radius value |
| l | liquid value |
| m | mixture value (lithium gas and noncondensible) |
| n | noncondensible value |
| o | wall outer radius value |
| p | pore value |
| s | solid value |
| sat | saturation value |
| sur | liquid–vapor surface value |
| v | wick inner radius value |
| w | wall value |
| $x, y$ | arbitrary species. |

Operators

| | |
|---|---|
| $\mathscr{L}(f)$ | linearization functional |
| $\delta A$ | time step or iterate difference, $A^{n+1} - A^n$ |
| $\Delta A$ | incremental change in variable $A$ |
| $\Omega(b)$ | function defined by equation (26) |
| $\langle A \rangle$ | average value of $A$ |
| $\mathbf{A}$ | vector quantity |
| $\nabla A$ | grad $A$ |
| $\nabla \cdot \mathbf{A}$ | div $\mathbf{A}$ |
| $\partial/\partial t(A)$ | partial derivative with respect to $t$ |
| $\partial/\partial z(A)$ | partial derivative with respect to $z$. |

to short-lived concentrated heat inputs, which could be caused by military attacks. The design concerns associated with space reactor heat pipes have provided the major impetus for increased accuracy and detail in transient heat pipe analysis.

The pioneering work in steady state heat pipe analysis was carried out by Cotter [7]. His work assumed steady state incompressible flow in both the liquid and the vapor regions with constant boundary conditions in the evaporator, adiabatic and condenser sections. His model predicted heat pipe fluid velocity and pressure profiles, as well as delineating some of the theoretical limits to heat pipe operation. In his vapor flow model, Cotter made use of the work of Yuan and Finkelstein [8] which describes pipe flow with injection or suction through a porous wall and expresses the axial pressure distribution in a polynomial of the radial Reynolds number. Slight modifications to Cotter's theory have been made since its publication, e.g. a correction concerning the proper location to equate the liquid and vapor pressures proposed by Ernst [9]. A more detailed steady state analysis was carried out by Busse [10] who made many of the same assumptions that Cotter did, but allowed for a radial variation of the axial velocity with a fourth-order polynomial. In later work, Busse and Prenger [11] describe the computer code AGATHE which expanded the velocity in an $n$-degree polynomial. Cotter's theory and some of the later modifications were implemented by Prenger in the computer code HTPIPE [12]. A similar steady state code named A-37 was written by Ernst [13]. Steady state heat pipe theory has been outlined in several texts [14–16].

With a desire to model transient effects, Cullimore [17] developed the computer code ASAHP which uses a thermal and flow resistance technique. The applicability of ASAHP to transient situations is limited because it assumes quasi-steady state hydrodynamics. Colwell and co-workers [18, 19] developed a two-dimensional $(r, z)$ finite difference model of the transient thermal behavior of low temperature heat pipes. His model does not include the hydraulic properties of heat pipe operation, but does have a thermal model for rewetting (which occurs after a section of the heat pipe has been boiled dry). Peery and Best [20] modeled a water heat pipe with mass, momentum and energy transfer using the Navier–Stokes equations. Their model included the vapor and wick regions, but assumed that vapor and liquid pressures are equal at the end of the condenser. Numerical problems were experienced because of their method of solution which decoupled the equations. Costello *et al.* [21] developed a program which models the transient behavior of high temperature heat pipes. Their program uses the Kachina method to determine the flow field characteristics and has some treatment of the solid startup phenomenon. Costello's code includes a rough treatment of noncondensible gas and the condenser pooling effect. The numerical method used to solve the flow equations is an explicit method which is iterated upon until convergence to an 'implicit' value.

The reactor transient code RELAP5 [22] has been adapted to heat pipe systems [23–25]. This adaptation, entitled ATHENA, uses a semi-implicit temporal discretization to solve the area averaged Navier–Stokes equations. ATHENA uses a volume-based capillary pressure relation to specify the liquid–vapor pressure difference, but it is evaluated explicitly. This has led to severe time step restrictions (much less than the Courant limit). The ATHENA model uses an area averaged pressure in both its continuity and energy equations, such that the liquid and vapor have different pressures only in the momentum equations.

The preliminary research for this paper [26–28] developed a detailed model of the vapor core of the heat pipe along with a more rudimentary wall/wick model. This model also used a semi-implicit discretization of the area averaged Navier–Stokes equations, including a noncondensible gas and the phenomenon of concentration driven mass diffusion. Conduction in the core gas was not modeled, and the wall/wick model was a lumped parameters thermal model. Severe time step restrictions were caused by a Fourier modulus limitation associated with the explicit discretization of the diffusion terms.

With the exception of the ATHENA code and the preliminary research for this paper, there has not been an accurate, detailed transient thermal hydraulic model of high temperature heat pipe response. The work that has been carried out by other researchers to date is either incomplete (Cullimore, and Colwell and co-workers include only transient thermal aspects) or numerically nonoptimal (Peery and Best, and Costello *et al.* both utilize deleterious numerical methods). The ATHENA code, the development of which is contemporary to this work, uses an accurate numerical scheme to determine the entire thermohydraulic behavior of the heat pipe. However, it does include diffusion and has no provision for solid lithium. It is subject to the small time steps necessary to ensure stability and accuracy because of the explicit capillary pressure relation discretization. The preliminary research for this paper included an accurate core model, but lacked axial conduction in the core, a hydraulic wick model, and a solid treatment. It was limited in time step size by the explicit diffusion discretization.

The previously mentioned transients of frozen startup, restart, and reaction to threats necessitate accurate, detailed modeling of the thermohydraulic behavior of both the wick and the core. Toward this end, the authors have developed the computer code THROHPUT (Thermal Hydraulic Response Of Heat Pipes Under Transients), which seeks to overcome the limitations of prior codes and to model the important phenomena of transient heat pipe behavior. (Previous descriptions of the THROHPUT code can be found in refs. [29, 30].) THROHPUT models the heat pipe using a fully implicit numerical technique that increases computational time per time step but removes most of the time step restrictions associated

with earlier codes, resulting in a net increase in computational speed. The physical processes treated in THROHPUT are: convection of mass, energy, and momentum; interphase and intraphase conduction; convective heat transfer; evaporation and melting; concentration driven mass diffusion; and capillary forces. Three phases and two components are modeled: the three phases of lithium and a noncondensible gas. This paper details the results of a sensitivity study which attempts to reproduce experimental data by varying the evaporation and condensation accommodation coefficients.

## 2. MODEL DESCRIPTION

### 2.1. *Assumptions*

The particular geometry chosen for the THROHPUT model coincides with that of the current designs for space reactor heat pipes [1, 31–35]. It consists of a cylindrical tube lined with an annular screen wick. The dimensions are user-specified. The model assumes lithium as a working fluid, where the lithium may exist as a solid, liquid, or gas. A noncondensible gas, assumed to be air, can be present in the vapor phase. The operating fluids can be changed by the suitable substitution of state relations. The lithium gas and the noncondensible are assumed to be intimately mixed, occupying the same volume with the same temperature at any particular location. It is usually assumed that the velocities of the two components are equal. In the THROHPUT code, the two gases are assumed to have different velocities, with the velocity difference described by the Dusty Gas Model [36]. Another common assumption in two-phase thermohydraulics is the equality of the liquid and vapor pressures, but such an assumption is not proper when capillary forces are the main driving forces of the system. In this case, the pressure difference between the liquid and vapor phases is related to the curvature of the interphasic meniscus.

In the absence of gravitational forces and azimuthally varying boundary conditions, flow in the heat pipe is entirely axial and radial. The major flow field is in the axial direction. With this in mind, the fluid equations are solved by area averaging over the radial and azimuthal directions, yielding a one-dimensional axial system. The important radial flows appear as interfacial terms associated with the evaporation and condensation processes and are treated in a separate radial model.

### 2.2. *Axial Model*

The main model in the THROHPUT code is the Axial Model. It consists of a set of 15 simultaneous partial differential equations which describe the behavior of the main system variables: density, pressure, temperature, velocity, and volume fraction for each of the four system components (lithium solid, liquid, and gas; and the noncondensible gas). The Axial Model equation set is (mixture denotes the mixture of lithium gas and noncondensible):

mixture continuity

$$\frac{\partial}{\partial t}(\alpha_m \rho_m) + \frac{\partial}{\partial z}(\alpha_m \rho_m V_m) = \sum_{x=l,s} \Gamma_{xg}; \quad (1)$$

noncondensible continuity

$$\frac{\partial}{\partial t}(\alpha_m \rho_m X_n) + \frac{\partial}{\partial z}(\alpha_m \rho_m X_n V_m) = \frac{\partial}{\partial z}\left(\alpha_m D_n^X \frac{\partial X_n}{\partial z}\right) + \frac{\partial}{\partial z}\left(\alpha_m D_n^p \frac{\partial \rho_m}{\partial z}\right); \quad (2)$$

liquid continuity

$$\varepsilon_v \frac{\partial}{\partial t}(\alpha_l \rho_l) + \varepsilon_v \frac{\partial}{\partial z}(\alpha_l \rho_l V_l) = \sum_{x=g,s} \Gamma_{xl}; \quad (3)$$

solid continuity

$$\varepsilon_v \frac{\partial}{\partial t}(\alpha_s \rho_s) = \sum_{x=g,l} \Gamma_{xs}; \quad (4)$$

mixture internal energy

$$\frac{\partial}{\partial t}(\alpha_m \rho_m U_m) + \frac{\partial}{\partial z}(\alpha_m \rho_m U_m V_m) = -P_m\left(\frac{\partial}{\partial z}(\alpha_m V_m) + \frac{\partial \alpha_m}{\partial t}\right) + \frac{\partial}{\partial z}\left(\alpha_m D_n^X (h_n - h_g)\frac{\partial X_n}{\partial z}\right) + \frac{\partial}{\partial z}\left(\alpha_m D_n^p (h_n - h_g)\frac{\partial \rho_m}{\partial z}\right) + \frac{\partial}{\partial z}\left(\alpha_m k_m \frac{\partial T_m}{\partial z}\right) + \sum_{x=l,s} (Q_{xm} + A_{xg}^{\Gamma}); \quad (5)$$

liquid internal energy

$$\varepsilon_v \frac{\partial}{\partial t}(\alpha_l \rho_l U_l) + \varepsilon_v \frac{\partial}{\partial z}(\alpha_l \rho_l U_l V_l) = -\varepsilon_v P_l\left(\frac{\partial \alpha_l V_l}{\partial z} + \frac{\partial \alpha_l}{\partial t}\right) + \varepsilon_v \frac{\partial}{\partial z}\left(\alpha_l k_l \frac{\partial T_l}{\partial z}\right) + \sum_{x=m,s,w} Q_{xl} + \sum_{x=g,s} Q_{xl}^{\Gamma}; \quad (6)$$

solid internal energy

$$\varepsilon_v \frac{\partial}{\partial t}(\alpha_s \rho_s U_s) = \varepsilon_v \frac{\partial}{\partial z}\left(\alpha_s k_s \frac{\partial T_s}{\partial z}\right) + \sum_{x=m,l,w} Q_{xs} + \sum_{x=g,l} Q_{xs}^{\Gamma}; \quad (7)$$

wall internal energy

$$\rho_w c_{p_w} \frac{\partial T_w}{\partial t} = \frac{\partial}{\partial z}\left(\alpha_w k_w \frac{\partial T_w}{\partial z}\right) + Q_{in} + \sum_{x=l,s} Q_{xw}; \quad (8)$$

mixture momentum

$$\frac{\partial}{\partial t}(\alpha_m \rho_m V_m) + \frac{\partial}{\partial z}(\alpha_m \rho_m V_m^2) = -\alpha_m \frac{\partial P_m}{\partial z} - \mathscr{F}_m V_m + \alpha_m \rho_m g_z ; \quad (9)$$

liquid momentum

$$\varepsilon_v \frac{\partial}{\partial t}(\alpha_l \rho_l V_l) + \varepsilon_v \frac{\partial}{\partial z}(\alpha_l \rho_l V_l^2) = -\varepsilon_v \alpha_l \frac{\partial P_l}{\partial z} - \mathscr{F}_l V_l - \Delta P_{cap}^v \frac{\partial \alpha_l}{\partial z} + \varepsilon_v \alpha_l \rho_l g_z ; \quad (10)$$

mixture state

$$P_m = \rho_m T_m (X_n R_n + (1 - X_n) R_g) ; \quad (11)$$

liquid state

$$\rho_l = \rho_l(P_l, T_l) ; \quad (12)$$

solid state

$$\rho_s = \rho_s(T_s) ; \quad (13)$$

volume fraction sum

$$\sum_{x = m,l,s} \alpha_x = 1 ; \quad (14)$$

capillary pressure relation

$$P_m - P_l = \mathscr{L}(\Delta P_{cap}(\alpha_m)) \quad (15)$$

where the system variables are: $\rho_m$, $\rho_l$, $\rho_s$, $X_n$, $\alpha_m$, $\alpha_l$, $\alpha_s$, $P_m$, $V_m$, $V_l$, $T_m$, $T_l$, $T_s$, and $T_w$. The interphase transfer terms ($\Gamma_{xy}$, $Q_{xy}$, $Q_{xy}^{\Gamma}$) are all functions of $\rho_m$, $X_n$, $T_m$, $T_l$, $T_s$, and $T_w$ and are defined in the Radial Model.

The axial model equation set is discretized using a staggered spatial mesh, with the conventional donoring and upwind differencing techniques. Temporal discretization is accomplished using a fully implicit scheme. This results in a nonlinear system which is solved using Newton's method. The Jacobian matrix for this system is block tridiagonal, with $15 \times 15$ blocks and as many blocks as there are axial nodes. Multiple passes are made through the system, updating the Jacobian at each pass, until the error norm of the variables is less than a user-specified value. This differs from the previous THROHPUT model [30], which made only one pass through the same system. The temporal discretization of the previous model was described as a linearized fully implicit model, and yielded the same accuracy with less stability. The main impetus behind going to a multiple pass technique was not the stability of the method, but rather the time step size. Multiple passes allow the updating of several highly nonlinear equations (namely, the mixture state equation and the capillary pressure relationship) and, thereby, the reduction of linearization error. Since the linearization error in these two equations was the limiting factor in time step control, eliminating the error was very attractive. The THROHPUT code is not limited by Fourier modulus or Courant limits due to the fully implicit temporal discretization scheme. Time step size is governed only by the ability to converge to a solution within the allowed number of passes, and by the preservation of the physical significance of the variables. However, the time step must also be small enough to capture the fluctuations of the heat input data.

### 2.3. *Radial Model*

The Radial Model was developed as a means of incorporating radial heat and mass transfer into the Axial Model. Its main objective is to provide interphase linkage terms to the Axial Model that are as implicitly determined as possible without sacrificing linearity. Interphase mass transfer between all of the phases is modeled. Melting and freezing are modeled with a discontinuous heat flux at the liquid–solid boundary. In order to simplify the Radial Model, some assumptions about the radial locations of the phases have been made. It is assumed that the phases exist in radial layers, in one of four specific configurations. These configurations represent the following conditions (see Fig. 2): cold state (all solid); startup or melting (liquid–solid); normal operation (all liquid); and shutdown or freezing (solid–liquid). The THROHPUT code assumes that the radial temperature distributions are parabolic in each nonvapor layer. The three coefficients for each region are determined by forcing the equations to satisfy boundary conditions and to match the average values computed in the Axial Model. This solution strategy gives a temperature distribution in each region which can be evaluated to yield the surface temperatures. If the crossover between two cases is overstepped, a rebalance is done after the time step that conserves both mass and energy.

### 2.4. *Axial Melt Front model*

Melt front propagation in the evaporator section is predominantly in the radial direction. After the initial melting of the evaporator section, the melt front progresses down the length of the heat pipe axially. This type of melt front is not accurately modeled with a radial propagation model, hence the development of an Axial Melt Front (AMF) model. The Radial Model is used twice by the AMF model: once for the liquid side and once for the solid side. The total heat and mass transfer for an AMF node is then determined by a volume weighted average of the two radial submodel results, along with some terms derived from a lumped parameters treatment of the axial interphasic boundary. Similar actions are taken when the axial melt front is coincident with a cell boundary.

### 2.5. *Surface model*

The heat pipe concept is based on the recirculation of the condensate liquid to the evaporator, which would be impossible without the capillary pressure head supplied by the wick. The capillary pressure relationship is therefore of utmost importance in heat pipe modeling. This relationship is

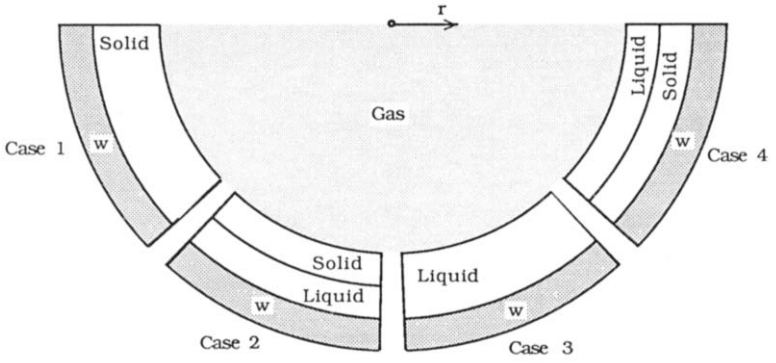


FIG. 2. Assumed phasic locations for the Radial Model.

$$P_m - P_l = \Delta P_{cap} = \frac{2\sigma}{r_c} = \frac{2\sigma\mu}{r_p} \tag{16}$$

where $r_c$ is the radius of curvature of the surface of the liquid–vapor interface. In order to make equation (16) as implicit as possible, the radius of curvature should be related to some other system variable. The resulting equation could be linearized to yield an implicit representation of the capillary pressure relationship fit for inclusion in the Axial Model equation set.

A geometric approach to modeling the radius is taken in lieu of methods commonly used by other researchers. Some of these methods set the liquid and vapor pressures equal at an assumed axial location and compute the phasic pressure distributions independently, which does not allow the capillary pressure difference to adjust to system parameters. There are two models for capillarity in the THROHPUT code: the Simplistic Model, which assumes azimuthal symmetry for all system variables, and the Horizontal Gravity Model, which includes the effects of terrestrial operation under a horizontal gravity field. The ATHENA code [24, 25] uses an approach similar to the Simplistic Model to determine the capillary pressure difference, but evaluates it explicitly.

### 2.6. *Vacuum treatment: the Dusty Gas Model*

In the initial stages of heat pipe startup, an effective vacuum ($\approx 10^{-4}$ Pa) exists in the vapor core region. The only specie present is the noncondensible gas. As the evaporator heats up and the vapor pressure of lithium increases, great density and concentration gradients are set up along the length of the heat pipe. Due to the extreme low pressure, the mass transport is governed by Knudsen diffusion, which occurs when the mean free path of a vapor molecule is much greater than the physical dimensions of the system. The THROHPUT code uses the Dusty Gas Model (DGM) as put forth by Cunningham and Williams [36]. The DGM provides for mass transfer due to both density and concentration gradients, and has been experimentally verified. The diffusive fluxes predicted by the DGM (after conversion into mass-based units and a mass average velocity) are

$$\mathbf{j}_A = -D_A^X \nabla X_A - D_A^p \nabla \rho_m \tag{17}$$

$$\mathbf{j}_B = -D_A^X \nabla X_B + D_A^p \nabla \rho_m \tag{18}$$

where

$$D_A^X \equiv D_{AB}^{\dagger} \rho_m [D_A^K m_B X_B^M + D_B^K m_A X_A^M] \tag{19}$$

$$D_A^p \equiv D_{AB}^{\dagger} [D_A^K m_B X_B^M X_A - D_B^K m_A X_A^M X_B] \tag{20}$$

$$D_{AB}^{\dagger} \equiv \frac{D_{AB}}{(m_A X_A^M + m_B X_B^M)(D_{AB} + D_A^K X_B^M + D_B^K X_A^M)} \tag{21}$$

and the mass fraction and mole fraction are represented by $X$ and $X^M$, respectively.

## 3. NET EVAPORATION RATE DETERMINATION

### 3.1. *Basic kinetic theory*

A crude formulation of the net evaporation flux from a surface is given by applying basic kinetic theory to the difference between the evaporating flux and the condensing flux [37]

$$\dot{m} = \dot{m}_e - \dot{m}_c = [2\pi R_g]^{-1/2} \left( \frac{P_{sat}(T_{sur})}{(T_{sur})^{1/2}} - \frac{P_g}{(T_g)^{1/2}} \right). \tag{22}$$

Making the assumption that $T_g \approx T_{sur}$

$$\dot{m} = [2\pi R_g T_{sur}]^{-1/2} (P_{sat} - P_g) \tag{23}$$

$$\equiv \beta (P_{sat} - P_g) \tag{24}$$

which defines the variable $\beta$.

Even if a gas is evaporating into a vacuum, there is a finite vapor density in front of the liquid surface. The crude model of the evaporation flux is modified to account for the recondensation of this vapor. Following Schrage [38], it is assumed that the vapor has a Maxwellian velocity distribution which is superimposed on an average velocity toward the surface.

The flux of this gas toward the surface is readily shown from kinetic theory to be

$$\dot{m}_c = \Omega(b)\beta P_g \tag{25}$$

where $b$ is the ratio of the overall speed to the most probable velocity of the gas, and $\Omega(b)$ is given by

$$\Omega(b) = e^{-b^2} + b\pi^{1/2}\{1 + \text{erf}(b)\}. \tag{26}$$

Approximations to this function are given by Collier [37] as

$$\Omega(b) = \begin{cases} 1 + b\pi^{1/2} & \text{for } b \ll 1 \\ 2b\pi^{1/2} & \text{for } b \gg 1. \end{cases} \tag{27}$$

Data in the transition range given by Collier have been fitted using a linear least squares method. Transition points are determined by equating the various lines. The resulting form is

$$\Omega(b) = \begin{cases} 1 + b\pi^{1/2} & \text{for } b < 0.1192 \\ 0.8959 + 2.6457b & \text{for } b \in (0.1192, 0.9962) \\ 2b\pi^{1/2} & \text{for } b > 0.9962. \end{cases} \tag{28}$$

The net evaporation flux is then

$$\dot{m} = \beta(P_{sat} - \Omega(b)P_g). \tag{29}$$

When a noncondensible gas is present, it is carried by the condensing specie to the surface, where it accumulates. The condensing gas must then diffuse through the noncondensible barrier in order to reach the surface. Collier [37] gives the following relationship for condensation in the presence of a noncondensible:

$$\dot{m} = \frac{H_{xm}(1 - X_n)}{c_{p_m}} \left\langle \frac{1}{P_n} \right\rangle \left( \frac{c_{p_m}\rho_m D_{gn}}{k_m} \right)^{2/3} \times (P_{sat}(T_{sur}) - P_g). \tag{30}$$

### 3.2. *Accommodation coefficients*

Equation (29) gives the net evaporation flux found by subtracting the maximum condensation flux from the maximum evaporation flux, the inherent assumption being that every atom that hits the surface condenses and every atom on the surface that evaporates remains in the vapor. Physically, this assumption is not valid: there are many phenomena that hinder the phase change process. Less than optimal evaporation and condensation fluxes are usually modeled with accommodation coefficients ($\sigma_e$ and $\sigma_c$) that vary from zero to one:

$$\dot{m} = \beta(\sigma_e P_{sat} - \sigma_c \Omega(b) P_g). \tag{31}$$

For most fluids, in most situations, the accommodation coefficients are assumed to be equal to one. However, for liquid metal evaporation from a wick surface in a cylindrical tube, the accommodation coefficients may be far from unity.

There are limited experimental data in the area of liquid metal condensation. Hsieh [39] cites the experimental results of a number of researchers who have found condensation heat transfer in liquid metals to be a fraction of the predictions of Nusselt theory (Misra and Bonilla, 5–15% of theory; Cohn, 1–13%; Englebrecht and Bonilla, 2–10%; Barry and Balzhiser, 9%). These consistently low condensation heat transfer coefficients can be translated directly into low condensation accommodation coefficients. Experimentally determined values for $\sigma_c$ and postulated temperature behavior for various liquid metals are shown in Fig. 3. Many of these researchers attribute the low condensation coefficients to the dimer content of the metal vapor. Most organic fluids, which do not exhibit low accommodation coefficients, are monatomic as a vapor. It is speculated that metal gases which exist as dimers might undergo a rate limiting reorientation upon condensation. Or, dimers might behave like a noncondensible or semicondensible gas and inhibit the condensation process by forming a barrier cloud over the condensing surface. The dimer content of a metal gas is a function of its temperature and pressure: the dimer model fraction of saturated lithium gas reaches 0.1 at 1500 K.

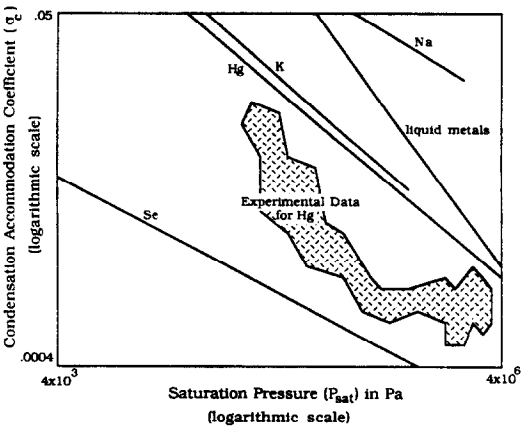


FIG. 3. Experimental and postulated variation of $\sigma_c$ with $T$ for various metal vapors (roughly redrawn from ref. [39]).

Huang (cited in ref. [39]) allows for the fact that certain molecules which hit the surface with low grazing angles were not condensed. His theoretical analysis determines the maximum value of $\sigma_c$ to be 0.88 instead of unity. Narusawa and Springer (cited in ref. [39]) find that the condensation accommodation coefficient depends upon surface contamination. For a clean surface, they find $\sigma_c > 0.67$, but for a contaminated surface their value for $\sigma_c$ is 0.16.

Somorjai [40] observes that the evaporation rate will be maximized if the activation energy for overcoming the attractive forces of the surface is less than the free energy of evaporation, such that the evaporation process itself is rate determining. Substances which undergo a reorientation during vaporization should exhibit an evaporation rate less than the maximum. Somorjai further states that, in some circumstances, an evaporating surface may have deep

cracks and crevices even if it is primarily flat. These inner channels may act as small Knudsen cells in which the evaporating molecules undergo many collisions before their final exit, providing a further resistance to vaporization. For a heat pipe with the liquid surface receding into the wick, it is easy to envision the macroscopic crevices (pores) and their related hindrance to evaporation.

In summary, the accommodation coefficient for liquid metal condensation ($\sigma_c$) in a heat pipe situation is affected by the following phenomena:

- Dimer content of the vapor. At higher temperatures, the dimer content of the vapor increases, which may necessitate an additional activation energy for reorientation upon condensation.
- Surface contamination. There is a large discrepancy between a screen wick surface and a flat interface.
- Surface grazing angle. During lithium heat pipe startups, the axial vapor velocity reaches large values, which tends to increase the number of particles that stick to the surface.

Similarly, the accommodation coefficient for liquid metal evaporation ($\sigma_e$) in a heat pipe situation is affected by the following phenomena:

- Surface recession into the wick. The further the liquid recedes into the wick, the greater the resistance to evaporation. A wick with less porosity would heighten the effect.
- Dimer content of the vapor. At higher temperatures, the dimer content of the vapor increases, which may necessitate an additional activation energy for reorientation upon evaporation.
- The local flow regime. A continuum flow situation would mitigate the influence of the reëntrant cylindrical geometry, whereas free molecular flow would encourage recondensation for all evaporating particles.

The THROHPUT code uses equation (31) to model the net evaporation rate. The evaporation flux is first converted to an evaporation rate (mass addition per volume)

$$\Gamma_{vg} = \dot{m}\frac{A_v}{V} = \frac{2r_v\varepsilon_s\beta}{r_i^2}(\sigma_e P_{sat} - \sigma_c\Omega(b)P_g) \quad (32)$$

where $\varepsilon_s$ is the fraction of the wick surface available for interphasic transport. The accommodation coefficients are input by the user and are constant for any given code run. Equation (30), which accounts for inhibition of the evaporation/condensation process due to the presence of a noncondensible, is used only if it predicts a value less than the maximum value predicted by kinetic theory. During the code runs executed to date, this condition has never occurred.

## 4. DISCUSSION OF RESULTS

### 4.1. *Problem setup*

The THROHPUT code has been set up to model a lithium heat pipe fabricated and tested at Los Alamos National Laboratory [41, 42], with the hope of reproducing results obtained experimentally. The design of the heat pipe is similar to those described in the literature [31–35]. The system dimensions as calculated from data in the aforementioned sources are

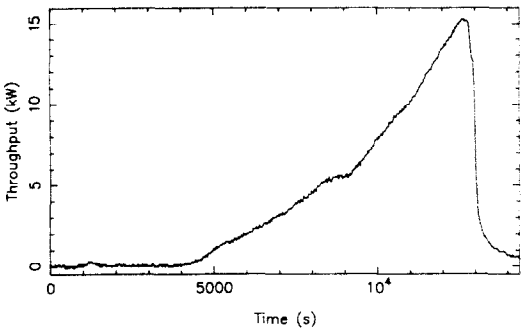


FIG. 4. Experimental heat throughput.

$$L_e = 0.4 \text{ m}, \quad L_a = 0.6 \text{ m}, \quad L_c = 3.0 \text{ m}$$

$$r_v = 7.136 \times 10^{-3} \text{ m}, \quad r_i = 8.000 \times 10^{-3} \text{ m}$$

$$r_o = 9.525 \times 10^{-3} \text{ m}, \quad \varepsilon_v = 0.682, \quad \varepsilon_s = 0.624$$

$$r_p = 5.3 \times 10^{-5} \text{ m}, \quad \varepsilon_0 = 0.6, \quad T_{amb} = 300 \text{ K}.$$

The heat pipe is assumed to be initially filled with a noncondensible gas at $1 \times 10^{-4}$ Pa and 300 K. The heat throughput as a function of time is set to the experimental value shown in Fig. 4. The only other data available for comparison from the experimental run is the time dependent temperature output of thermocouples located at various locations along the heat pipe.

In most of the code runs, there are 25 axial nodes: 5 in the evaporator, 5 in the adiabatic section, and 15 in the condenser. The maximum time step is set to 10 s, the maximum number of passes through the Jacobian matrix during any time step is set to 20 and the maximum tolerable error norm for convergence tests is $10^{-4}$. Most of the code runs are made with no diffusion, standard gas friction factors, and the Horizontal Gravity Model for capillarity.

### 4.2. *Accommodation coefficient grid search*

The accommodation coefficients, $\sigma_e$ and $\sigma_c$, are functions of many system variables (see Section 3.2). The particular functional dependence is unknown. The THROHPUT code assumes that the accommodation coefficients are constant for a given code run.

Many code runs have been executed to determine the effect of changing the accommodation coefficients on system parameters. The $(\sigma_e, \sigma_c)$ space is spanned by a $6 \times 6$ grid, where both coefficients take on the values: (0.01, 0.1, 0.3, 0.5, 0.7, 1.0). A schematic of

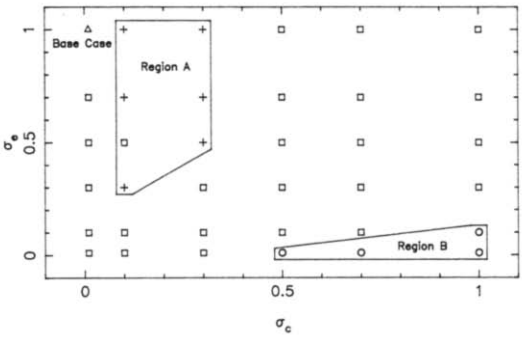


FIG. 5. Accommodation coefficient search grid.

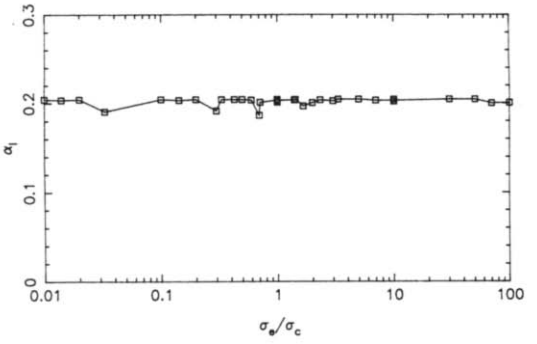


FIG. 6. Liquid volume fraction vs $\sigma_e/\sigma_c$ at time 1.

this grid is shown in Fig. 5. This grid is searched with two main objectives: to duplicate experimental data as closely as possible, and to conform to expected physical behavior.

A code run normally generates values for all the system variables at each nodal point at any desired output time. In the grid search there are 36 code runs. Such an inundation of data is difficult to assimilate at once, hence a concise quantification of the two objectives has been formulated.

(1) Evaporator exit temperature is compared to the experimental value (at two model times, 4529 and 8999 s).

(2) Melt front position is compared to a melt front position calculated using experimental temperature values (at two model times, 4529 and 8999 s).

(3) Liquid volume fraction in node 1, at the evaporator end of the heat pipe, is examined to determine proximity to the value necessary for continued heat pipe operation (at two model times, 4529 and 8999 s).

The times of comparison are chosen to correspond with experimental output times early and late in the transient. The first time is soon after the transient has started in earnest ($Q_T = 400$ W). The second time is well into the transient ($Q_T = 5500$ W), as is indicated by the fact that several of the grid search runs are fully molten by then.

The following sections describe the results of the grid search for each of the six criteria in relation to the experimental or expected values. An important parameter in describing the effects of varying the accommodation coefficients is their ratio, $\sigma_e/\sigma_c$. Rearranging equation (31) gives

$$\dot{m} = \beta\sigma_c\left(\frac{\sigma_e}{\sigma_c}P_{sat} - \Omega(b)P_g\right) \tag{33}$$

$$\equiv \beta\sigma_c([P_{sat}]_{eff} - \Omega(b)P_g). \tag{34}$$

The accommodation coefficient ratio serves as a multiplier for the saturation pressure, which causes a marked change in the latent heat transfer in the heat pipe. The $\sigma_c$ factor in this equation does not change the equilibrium saturation pressure, but rather the rate at which the system approaches homeostasis.

The code runs for the grid search met with varying degrees of success. Each of these runs was able to model out to the first output time. The second output time was reached by 26 of the 36 runs. Of the ten runs that did not model all the way to the second output time, six runs did not finish because the liquid volume fraction in node 1 went to zero, signifying insufficient liquid return. These six runs are marked by a + in Fig. 5, Region A. All of the six runs modeled past 8400 s, and their results are included as complete runs. The remaining four runs are incomplete because condensation rates were extremely high, forcing the time step to be reduced accordingly. Run times became prohibitive and the decision was made to discontinue the modeling. These four runs are marked by a circle in Fig. 5, Region B. The results from the runs in Region B are included in the plots, but are marked as incomplete runs.

The data in this section is presented in two different formats. The first consists of the variable in question plotted against the accommodation coefficient ratio ($\sigma_e/\sigma_c$). The ratio axis is plotted logarithmically, as the ratio values span four cycles. Secondly, this variable is displayed vs $\sigma_c$ for lines of constant $\sigma_e$.

In some of the graphs, the experimental value is displayed. Since the experimental value does not depend on the $x$-axis, it shows up as a horizontal line. Roughly estimated error bars on the experimental values are shown.

4.2.1. *Liquid volume fraction.* The liquid volume fraction in the first node serves as an indicator of the efficiency of the liquid return mechanisms. If the liquid capillary pressure head (both normal and axial) is insufficient to make up the liquid volume lost to evaporation, the liquid level in the evaporator decreases until it reaches zero. In an ideal situation, the liquid level does not vary greatly from the nominal value (which is $\alpha_l \approx 0.2043$ for the present model).

At the first comparison time, the liquid volume fractions for the various grid positions are all close to the nominal value (see Fig. 6). This output time is so near the beginning of the transient that the liquid return has been sufficient to keep up with the evaporation for all of the grid points, primarily because evaporation rates are still low.

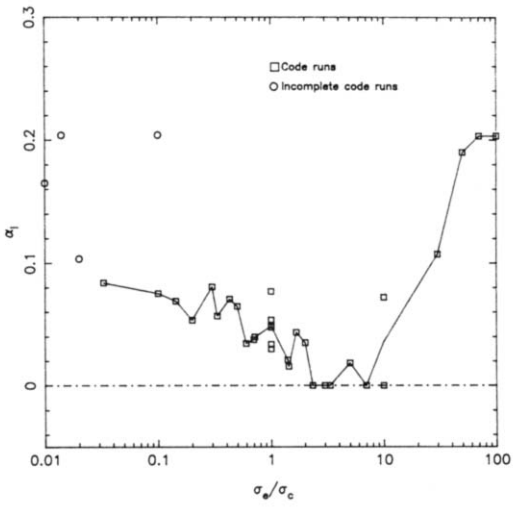


FIG. 7. Liquid volume fraction vs $\sigma_e/\sigma_c$ at time 2.

By the second comparison time, the significant differences between the effective saturation pressures of the grid points have become apparent in the liquid return capability. Indeed, several of the runs are terminated prematurely due to dryout of the liquid region. Figure 7 shows the variation with respect to the accommodation coefficient ratio (and in turn, to $[P_{sat}]_{eff}$). Varying the effective saturation pressure produces two competing effects.

(1) The gas pressure is determined by the saturation pressure corresponding to the local liquid surface temperature, due to the small time constant for the evaporation process. The liquid pressure is usually equal to the gas pressure at the melt front, due to pooling in the vapor core, and is therefore a strong function of the melt temperature. The liquid pressure at the melt front represents the maximum liquid return pressure drop, unless there is also pooling closer to the evaporator section (where the temperatures and pressures are higher). This last condition does not usually occur, as the excess pressure tends to direct liquid flow back toward the melt front (i.e. an unstable situation). The maximum liquid return pressure is then approximately equal to the effective saturation pressure at the melt temperature. High values of the accommodation coefficient ratio therefore lead to large liquid return pressures.

(2) Low ratios lead to low effective saturation pressures and consequently, low evaporation rates. Low evaporation rates eliminate the need for liquid return, which implies that high ratios are detrimental to the liquid return process. This effect is directly opposed to the first effect.

Figure 7 can be explained in terms of three areas.

(1) For low ratios, $\sigma_e/\sigma_c < 1$, the physical processes outlined in 2 above dominate. There is little need for liquid return, and the fact that liquid return is minimal does not matter. The figure shows that $\alpha_l \approx 0.10$, or half of the nominal value, which signifies that the evaporator is still losing liquid despite the influence of the second effect.

(2) For $\sigma_e/\sigma_c \in (1, 10)$, effects 1 and 2 are both important. The accommodation coefficient ratio is high enough such that evaporation rates are high, yet low enough such that liquid return pressures are inadequate. The worst problems with liquid return are experienced here; the six code runs that go to zero liquid volume fraction are in this area.

(3) For high ratios, $\sigma_e/\sigma_c > 10$, the first effect dominates (liquid return pressures are high enough to overcome the excess demand for liquid caused by the high evaporation rate). In fact, these code runs have an extra benefit: in most of these runs, the heat pipe is completely molten by the second comparison time, indicating that the maximum liquid return pressure is set by the saturation pressure at a temperature higher than the melt temperature (which results in a larger return pressure). The figure shows that the liquid volume fraction is at the nominal level and, since the pipe is fully molten, it could probably remain at this level if the throughput continued to increase.

The result of the grid search with respect to the liquid volume fraction is that the accommodation coefficient ratio should be large ($> 10$) for liquid levels to conform to expected heat pipe behavior.

4.2.2. *Melt front position.* During the heat pipe startup transient, the melt front progresses radially through the evaporator section, and then axially down the length of the pipe. The axial melt front (AMF) position is an indication of the heat transfer rate down the pipe.

There is no experimental measurement of the melt front position, per se, but its location may be inferred from a linear interpolation of the experimentally measured temperature distribution. The experimental temperatures and their locations are known relatively accurately: there is little error in the endpoints of the linearization. The main error in the experimental determination of the melt front location is the linearization process itself: temperature distributions around the melt front are far from linear.

Numerically, the melt front determination is made with volume fractions in the AMF model. However, the AMF could be determined in a manner similar to the experimental method. The two methods are compared to get an estimate of the error in linearization (relative to the linearization distance) which is assumed to apply to the experimental linearization process as well. This is merely a rough estimate of the experimental error in determining the melt front position; there is no confidence level associated with this error bar.

Figure 8 shows the melt front position at the first comparison time plotted vs $\sigma_c$. Definite trends can be observed.

- Melt front position decreases with increasing $\sigma_c$; they are inversely related.

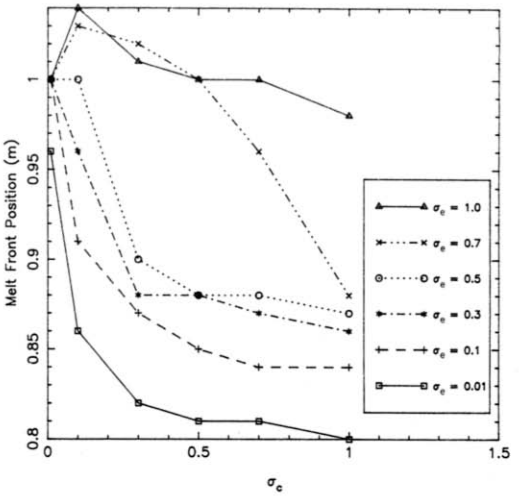


FIG. 8. Axial melt front position vs $\sigma_c$ at time 1.

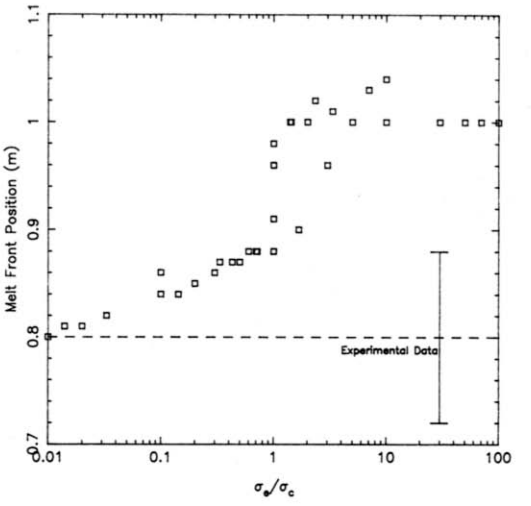


FIG. 9. Axial melt front position vs $\sigma_e/\sigma_c$ at time 1.

- Melt front position increases with increasing $\sigma_c$; they are directly related.

Another phenomenon can be observed in this figure, of numerical rather than physical origin. When an AMF is progressing down the pipe, there is a numerically induced tendency to spend more time at the node boundaries than inside a node. This occurs because an AMF within a node is generally between a solid and a liquid phase which are both very close to the melt temperature; thus the AMF moves rapidly. If an AMF is coincident with a cell boundary, the solid node may be well below the melt temperature. The AMF will then move a small distance into the solid node, only to be subsequently pushed back to the boundary on the next time step, leaving the solid a little warmer in the exchange. This process continues until the solid node gets close enough to the melt temperature for the AMF to progress through the node, which occurs rapidly as previously stated. The conservation of energy in the wick causes the average rate at which the AMF moves down the pipe to be correct, even though the instantaneous AMF velocity curve may have a sawtooth shape. This numerical phenomenon does *not* cause the AMF to exist only at the boundaries: the process has been exaggerated for the sake of discussion. In Fig. 8, the node boundaries are located at 0.88 and 1.0 m, where a large number of the melt fronts are also located.

Figure 9 shows the same data plotted vs the accommodation coefficient ratio. The two trends observed on the previous figure are summed up in this plot: the melt front position increases with increasing ratio. This result is intuitively expected. The primary heat transfer mechanism in the heat pipe is due to the latent heat of the vapor. Increasing the ratio increases the saturation pressure and enhances transfer of the latent heat necessary to move the melt front down the pipe. The experimental melt front position (with roughly estimated error bars) is also shown. The error bars are quite large in comparison with the spread of the numerical results, such that any ratio less than unity would fall within the tolerance.

By the second comparison time, the lines of constant $\sigma_e$ on the melt front position vs the $\sigma_c$ plot are more similar to one another in shape (see Fig. 10). The same tendencies that were observed in Fig. 8 are seen here: the melt front is directly related to $\sigma_e$ and inversely related to $\sigma_c$. The experimental melt front position is also displayed (sans error bars since they were too small to be seen on this figure). The experimental value can be duplicated by several combinations of accommodation coefficients.

Figure 11 shows the same data plotted vs the ratio. The dependence of the melt front position on the accommodation coefficient ratio is easily discerned. The graph also shows that several of the code runs have advanced to the extent that they are completely molten (AMF at 4.0 m). In order to match the exper-

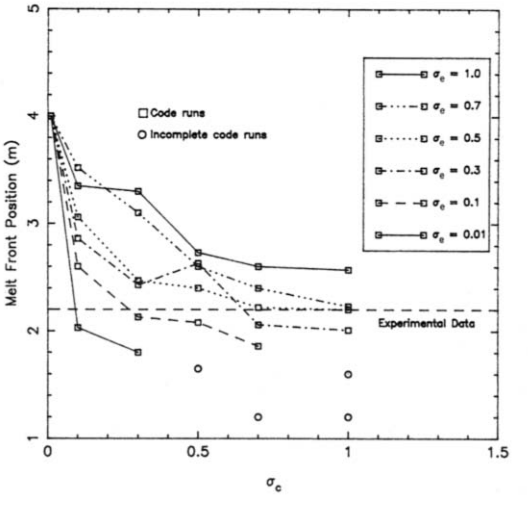


FIG. 10. Axial melt front position vs $\sigma_c$ at time 2.

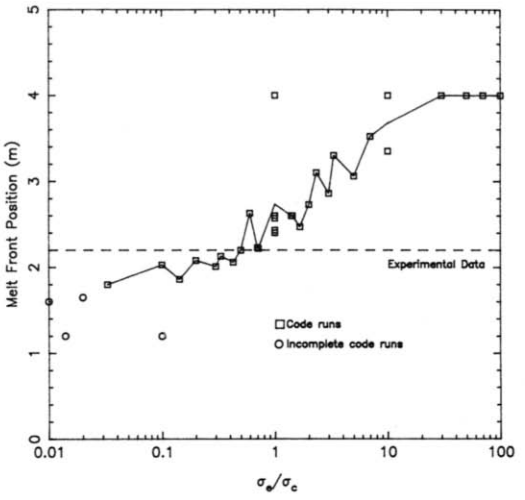


FIG. 11. Axial melt front position vs $\sigma_e/\sigma_c$ at time 2.

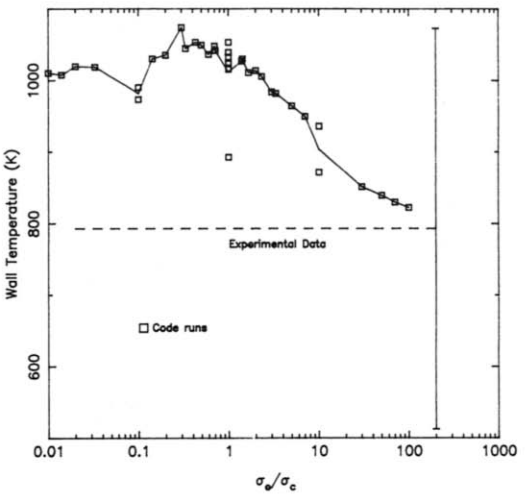


FIG. 13. Wall temperature at the evaporator exit vs $\sigma_e/\sigma_c$ at time 1.

imental data, the ratio must be in the range from 0.1 to 1.0.

4.2.3. *Wall temperature at the evaporator exit.* The experimental wall temperature at the evaporator exit is obtained from the average output of two thermocouples, one located on the top and one on the bottom of the heat pipe. At the first comparison time, there is a great disparity between the readings of the two thermocouples: the upper one reads a temperature 560 K greater than the lower one. It is postulated that the hot gas from the evaporator is heating up the top while the cooler liquid is against the bottom. At the second comparison time, the difference between the two readings is much less: 18 K. The error bars on the figures are set equal to the temperatures that were averaged.

The variation of wall temperature at the evaporator exit with $\sigma_c$ is shown in Fig. 12. A strong dependence

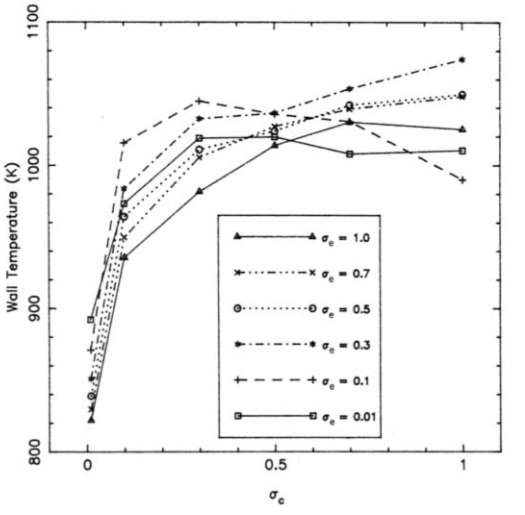


FIG. 12. Wall temperature at the evaporator exit vs $\sigma_c$ at time 1.

is exhibited: wall temperature increases with increasing $\sigma_c$ and, for low $\sigma_c$, wall temperature drops significantly. A weaker dependence on $\sigma_e$ is indicated, with the primary effect being a change in the overall shape of the curve. The condensation accommodation coefficient is proportional to the condensing flux; hence when it goes to zero the vapor does not condense. If condensation is decreased, the vapor travels further down the pipe before depositing its energy, thereby flattening out the axial temperature distribution and decreasing the evaporator exit temperature, which is the effect shown in the figure.

Figure 13 shows the same data plotted with respect to the accommodation coefficient ratio. A general trend of decreasing wall temperature with increasing ratio (for ratio values greater than unity) can be seen, primarily caused by the extreme dip in temperature at low $\sigma_c$ already noted. Below a ratio value of unity, there is no definite variation of wall temperature with ratio. Also included is the experimental value with its error bars, which was omitted from the previous figure in order to show greater detail. The large error bars encompass all of the code run results, leading to no clear conclusion concerning which ratio is desired to match the experiment.

The second comparison time results show a definite, almost functional, relationship between evaporator exit wall temperature and both of the accommodation coefficients (see Fig. 14). As in the first time results, the temperature increases with increasing $\sigma_c$, still showing the extreme drop in temperature at low $\sigma_c$. In contrast to the first time results, there is also a strong temperature–$\sigma_e$ relationship: temperature increases with decreasing evaporating coefficient. The experimental value is known far more accurately and can be reproduced numerically with several $(\sigma_e, \sigma_c)$ combinations.

These data are perhaps even more revealing when plotted vs the accommodation coefficient ratio (see Fig. 15). All of the code run results lie on a gently

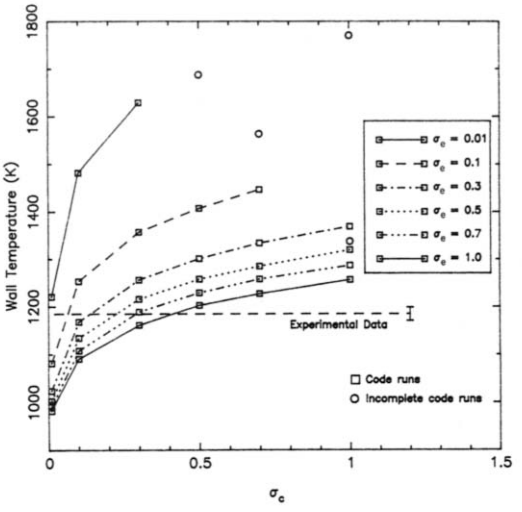


FIG. 14. Wall temperature at the evaporator exit vs $\sigma_c$ at time 2.

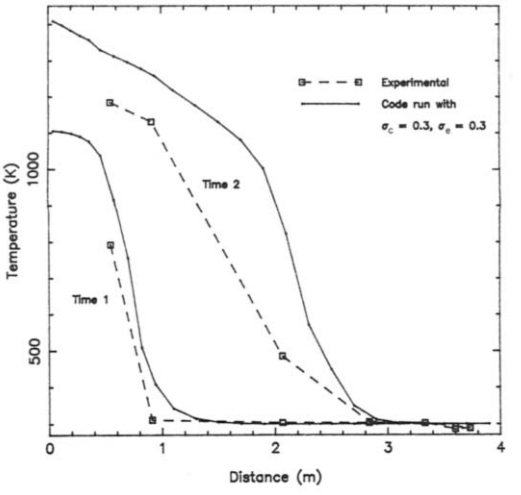


FIG. 16. Comparisons of the experimental wall temperature distribution with the best compromise code run ($\sigma_e = 0.3$, $\sigma_c = 0.3$).

sloping curve, the temperature varying from 1000 to 1800 K over the four cycles of the ratio. The smoothness and exactness of this relationship is in contrast to the jaggedness of the liquid volume fraction or the melt front position relationships at the second comparison time, suggesting less dependence on the numerics of the solution and more dependence on the physics of the situation. Including the effects of the error bars, the experimental value can be reproduced with a ratio somewhere between 2 and 3.

The underlying reason for the incomplete code runs is most apparent on this figure. The evaporator exit temperatures for the incomplete runs are extremely high and, since the amount of heat throughput is a constant for all of the runs, the temperatures in the rest of the pipe are correspondingly low. The temperature disparity between the hot gas and the cool condensing surface causes a situation which is difficult to model: the large condensation rates remove more of the lithium gas from the vapor phase than is present unless the time step is very small. The time step is restricted to the point that the solution proceeds with excruciating slowness, hence the termination of these runs before completion. The exit temperatures for the incomplete runs all lie below the curve in Fig. 15, which is expected because the exit temperature increases with time.

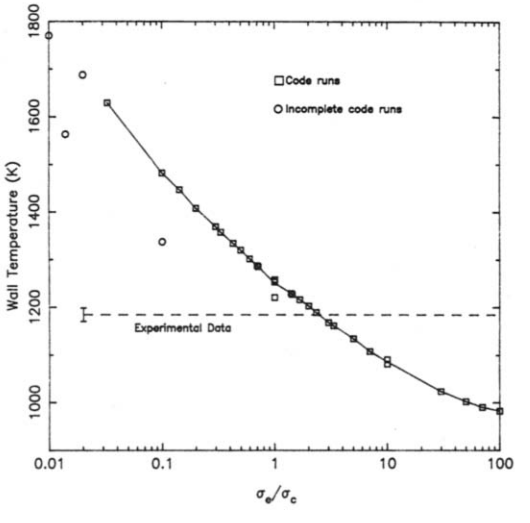


FIG. 15. Wall temperature at the evaporator exit vs $\sigma_e/\sigma_c$ at time 2.

4.2.4. *Conclusions.* The examination of each of the variables in the search of the accommodation coefficient grid has yielded preferred values of the coefficients for agreement with experimental results or expected behavior.

- Liquid volume fraction: to conform with expected behavior, the accommodation coefficient ratio must be greater than 10.
- Melt front position: to match experimental values, the ratio must be between 0.1 and 1.
- Evaporator exit wall temperature: to agree with experiment, the ratio must be between 2 and 3.

The three criteria on the ratio are disjoint: only one may be satisfied at a time. This indicates that the initial assumption that the accommodation coefficients could be modeled as constants, instead of spatially varying functions, was incorrect. To reproduce the experimental data and to conform to expected heat pipe behavior, the coefficients should depend on temperature, liquid level, wick porosity, gas velocity and gas flow regime (see Section 3.2).

Although the three criteria may not be strictly satisfied simultaneously, the code run which sets both accommodation coefficients equal to 0.3 forms the best compromise. Liquid return is still very small for this run ($\alpha_l$ at node 1 is 0.0337), but the temperature distribution compares favorably with the experimental temperature distribution at time 2 (see Fig. 16). Figure 17 shows how the temperature distribution

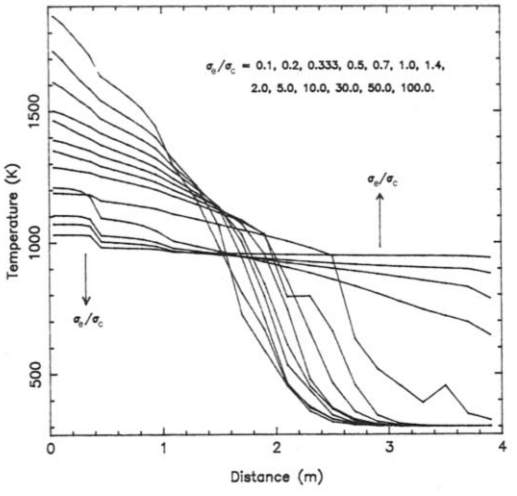


FIG. 17. Wall temperature distributions for various accommodation coefficient ratios at time 2.

is affected by changes in the accommodation coefficient ratio.

## 5. SUMMARY

### 5.1. *Virtues of the model*

The THROHPUT code is the only code in existence that can execute a detailed, fully transient model of the startup of a liquid metal heat pipe from a frozen solid condition to steady state operation. It models heat, mass, and momentum transfer between four components: lithium solid, lithium liqiud, lithium vapor and a noncondensible gas. The THROHPUT code uses a fully numerical technique which makes time step sizes greater than the Courant limit possible. The code makes no assumptions concerning the location of pressure equality between the liquid and the vapor; it has two models for wick capillarity, both of which are evaluated implicitly. Both capillarity models handle pooling into the core and recession into the wick, and one model includes the effects of azimuthal asymmetry due to horizontal gravity. The pooling into the core is handled in a natural manner, with no artificial 'pooling nodes' and no difficulties in liquid inventory estimation. The THROHPUT code contains a model which uses radial parabolic temperature distributions to estimate the interphasic heat and mass transfer rates. The Radial Model is combined with a lumped parameters axial treatment to model the progression of the melt front axially. Mass transfer by gaseous diffusion, axial capillary forces, and the effects of radial mass injection and suction on the axial gas flow friction are also included in the THROHPUT code.

### 5.2. *Limitations of the model*

Any model must make some concessions if it is to accomplish its modeling goals without undue complexity. A successful model is one that takes into account all of the physical phenomena necessary to describe every anticipated condition, and concurrently realizes its own limitations. Some of the physical conditions that are not modeled in the THROHPUT code are: boiling in the wick; supersonic vapor flow; alternate wick geometries and working fluids; entrainment of the liquid phase in the vapor phase; and interphasic drag.

The THROHPUT code has been determined to be very sensitive to the values chosen for the accommodation coefficients ($\sigma_e$ and $\sigma_c$) in the net evaporation rate equation

$$\dot{m} = [2\pi R_g T_{sur}]^{-1/2}(\sigma_e P_{sat} - \sigma_e \Omega(b) P_g). \quad (35)$$

An effort has been made to match experimental melt front locations and evaporator exit temperatures while ensuring adequate liquid return by varying the accommodation coefficients. Each of these criteria can be satisfied by the proper choice of coefficients, but no pair of coefficients is found that meets all of the requirements simultaneously. The ratio of the accommodation coefficients, $\sigma_e/\sigma_c$, is determined to have more influence on the modeling results than the values of the individual coefficients. An effective saturation pressure which multiplies the standard saturation pressure by the accommodation coefficient ratio is defined.

### 5.3. *Recommendations for future work*

Further experimentation in a number of areas should be conducted in order to provide insight into some of the basic physics of heat pipe operation. Greater instrumentation during heat pipe experimental transients, including intrusive monitoring, is needed. Specifically, measurements of pressures and velocities for both the liquid and the gas at various axial locations are required. Knowledge of the liquid level would also be instructive; perhaps this could be obtained with a transmission gamma radiation gauge. Additional thermocouples along the heat pipe would facilitate experimental tracking of the axial melt front.

Separate experiments could be carried out to quantify the capillary pressure relationship. Ransom [43] has proposed an experimental setup where liquid level could be adjusted (and measured) using a piston while the capillary pressure difference is monitored. The surface properties of an implanted wick structure could be studied, including recession into the wick and the hysteresis of pooling. Further investigation into capillary surface properties could be accomplished by modifying Ransom's proposed apparatus. Evacuation of the overgas could show the capillary behavior at low pressures, similar to the startup pressures of liquid metal heat pipes. The installation of a multilayer screen wick could provide for demonstrations of the fluctuations in pressure difference during liquid recession. Additional information could be gained by conducting the experiment in the absence of gravity, in an airplane executing a free fall or on the space shuttle. In addition to this

experiment, the validity of the axial capillary force term could be explored by observing the flow of liquid through a porous medium in zero gravity.

Experimentation concerning the dependence of the accommodation coefficients on system parameters is needed. In particular, the dependencies mentioned in Section 3.2 should be examined. Tests of two varieties could be performed: steady state tests in which the effective saturation pressure for various situations is measured; and instantaneous rate tests in which the evaporation/condensation process is allowed to continue for a short period of time before being halted to determine the state of the system. The length of time necessary for the rate tests would be dependent upon the accuracy of the measuring process (the amount of liquid or the amount of gas present at the beginning and at the end of the test would have to be measured), the minimization of startup and shutdown end effects on the test, and the magnitude of the evaporation rate itself. The difficulties in measuring the phasic masses and the rapid rate at which the system goes to steady state may preclude instantaneous rate tests altogether. Nevertheless, the results of this paper indicate that there is a greater need for steady state tests, as the effective saturation pressure is much more pivotal to heat pipe behavior than the time constant for the mass exchange process. Steady state tests should be conducted which measure the effective saturation pressure as a function of temperature, liquid recession into a wick structure and the average grazing angle of the gas with respect to the surface. This last parameter could be varied by changing the velocity of a gas jet directed over the condensing surface. While the capillarity tests could be carried out using water or a freon, the evaporation/condensation tests should be executed with a liquid metal working fluid, inasmuch as the molecular properties of ionicly bonded species differ significantly from those of covalently bonded species. The ultimate objective of the evaporation/condensation tests is to determine functional forms for the accommodation coefficients which incorporate the relevant physical phenomena and can be easily applied to heat pipe modeling.

*Acknowledgment*—The research was performed under appointment to the Nuclear Engineering, Heat Physics, and Radioactive Waste Management Fellowships program administered by Oak Ridge Associated Universities for the U.S. Department of Energy.

## REFERENCES

1. J. E. Boudreau and D. Buden, A new generation of reactors for space power. In *Proc. Symp. on Advanced Reactor Systems*, CONF-821148-Summs., Washington, DC, 15–17 November (1982).
2. P. W. Garrison and K. T. Nock, Nuclear electric propulsion (NEP) spacecraft for the outer planet orbiter mission. In *Proc. AIAA/SAE/ASME 18th Joint Propulsion Conf.*, AIAA-82-1276, Cleveland, Ohio, 21–23 June (1982).
3. R. G. Palmer, L. B. Lundberg, E. S. Keddy and D. R. Koenig, Nuclear Reactor System Study for NASA/JPL, Final Report, LA-9498-MS, Los Alamos National Laboratory, Los Alamos, New Mexico (1982).
4. F. C. Prenger and J. A. Sullivan, Conceptual designs for 100-MW space radiators. In *Proc. Advanced Nuclear Systems Symp.*, CONF-821103-Summs., LA-UR-82-3279 (1982).
5. W. A. Ranken, Status of high-temperature heat pipe technology. In *Proc. National Research Council Symp. on Advanced Reactor Systems*, Washington, DC, 15–17 November (1982).
6. W. A. Ranken, Space reactors, October 1981–March 1982, Program Report LA-9598-PR, Los Alamos National Laboratory, Los Alamos, New Mexico (1983).
7. T. P. Cotter, Theory of heat pipes, LA-3246-MS, Los Alamos Scientific Laboratory, Los Alamos, New Mexico (1965).
8. S. W. Yuan and A. B. Finkelstein, Laminar pipe flow with injection and suction through a porous wall, *ASME Trans.* **78**, 719–724 (1956).
9. D. M. Ernst, Evaluation of theoretical heat pipe performance. In *Proc. Thermionic Conversion Specialist Conf.*, Palo Alto, California, 30 October–1 November, pp. 349–354 (1967).
10. C. A. Busse, Pressure drop in the vapor phase of long heat pipes. In *Proc. Thermionic Conversion Specialist Conf.*, Palo Alto, California, 30 October–1 November, pp. 391–398 (1967).
11. C. A. Busse and F. C. Prenger, Numerical analysis of the vapour flow in cylindrical heat pipes. In *Proc. Fifth Int. Heat Pipe Conf.*, Tsukuba Science City, Japan, 14–18 May (1984).
12. F. C. Prenger, *Heat Pipe Computer Program (HTPIPE) User's Manual*, LA-8101-M, Los Alamos National Laboratory, Los Alamos, New Mexico (1979).
13. D. M. Ernst, Study of a heat rejection system for the nuclear electric propulsion (NEP) spacecraft, NASA-CR-169921, Jet Propulsion Laboratory, Pasadena, California (1983).
14. S. W. Chi, *Heat Pipe Theory and Practice*. Hemisphere, New York (1976).
15. D. Chisholm, *The Heat Pipe*. Mills & Boone, London (1971).
16. P. Dunn and D. A. Reay, *Heat Pipes*. Pergamon Press, Oxford (1976).
17. B. A. Cullimore, Modeling of transient heat pipe effects using a generalized thermal analysis program. Presentation to the Transient Heat Pipe Modeling Workshop, Los Alamos, New Mexico, 4–5 March (1986).
18. W. S. Chang and G. T. Colwell, Mathematical modeling of the transient operating characteristics of a low-temperature heat pipe, *Numer. Heat Transfer* **8**, 169–186 (1985).
19. G. T. Colwell and C. Camarda, Heat pipe modeling and experimental data. Presentation to the Transient Heat Pipe Modeling Workshop, Los Alamos, New Mexico, 4–5 March (1986).
20. J. Peery and F. Best, Simulation of heat pipe rapid transients. Presentation to the Transient Heat Pipe Modeling Workshop, Los Alamos, New Mexico, 4–5 March (1986).
21. F. A. Costello, M. Merrigan and T. R. Scollon, Jr., Detailed transient model of a liquid-metal heat pipe. Presentation to the Transient Heat Pipe Modeling Workshop, Los Alamos, New Mexico, 4–5 March (1986).
22. V. H. Ransom *et al.*, *RELAP5/MOD2 Code Manual, Volume 1: Code Structure, System Models and Solution Methods*, EGG-SAAM-6377. Idaho National Engineering Laboratory, EG&G Idaho, Inc., Idaho Falls, Idaho (1984).
23. C. D. Fletcher and H. Chow, Simulation of the General Electric SP-100 space reactor concept using the ATHENA computer code. In *Trans. 3rd Symp. on*

*Space Nuclear Power Systems*, CONF-860102-Summs., Albuquerque, New Mexico, 13–16 January (1986).
24. V. H. Ransom, ATHENA heat pipe model. Presentation to the Transient Heat Pipe Modeling Workshop, Los Alamos, New Mexico, 4–5 March (1986).
25. V. H. Ransom, Some new directions in system transient simulation. In *Proc. Second Int. Conf. on Simulation Methods in Nuclear Engineering*, Montreal, Canada, 14–16 October (1986).
26. M. L. Hall, Computer modeling of the transient thermohydraulic behavior of a high temperature heat pipe for space reactor applications. Presentation to the Transient Heat Pipe Modeling Workshop, Los Alamos, New Mexico, 4–5 March (1986).
27. M. L. Hall and J. M. Doster, Transient modeling of the thermohydraulic behavior of high temperature heat pipes for space reactor applications. In *Proc 14th Space Simulation Conf.*, Baltimore, Maryland, 3–6 November, pp. 313–330 (1986).
28. M. L. Hall and J. M. Doster, Transient thermohydraulic heat pipe modeling. In *Trans. 4th Symp. on Space Nuclear Power Systems*, Albuquerque, New Mexico, 12–16 January, pp. 407–410 (1987).
29. M. L. Hall and J. M. Doster, Transient thermohydraulic heat pipe modeling. In *Space Nuclear Power Systems 1987* (Edited by M. S. El-Genk and M. D. Hoover). Orbit, Malabar, Florida (1987).
30. M. L. Hall and J. M. Doster, The THROHPUT code: thermohydraulic heat pipe modeling. In *Trans. 5th Symp. on Space Nuclear Power Systems*, Albuquerque, New Mexico, 11–14 January (1988).
31. E. S. Keddy and H. E. Martinez, Development of high temperature liquid metal heat pipes for isothermal irradiation assemblies. In *Proc. 17th Intersociety Energy Conversion Engineering Conf.*, Los Angeles, California, August (1982).
32. M. A. Merrigan, J. E. Runyan, H. E. Martinez and E. S. Keddy, Development and test of a space-reactor-core heat pipe. In *Proc. AIAA 18th Thermophysics Conf.*, Montreal, Quebec, 1–3 June (1983).
33. M. A. Merrigan, H. E. Martinez, E. S. Keddy, J. Runyan and J. E. Kemme, Performance demonstration of a high-power space-reactor heat-pipe design. In *Proc. 18th Intersociety Energy Conversion Engineering Conf.*, Orlando, Florida, 21–26 August (1983).
34. M. A. Merrigan, E. S. Keddy, J. Runyan and H. E. Martinez, Development and extended operation of a high power radiation loaded heat pipe. In *Proc. 19th AIAA Thermophysics Conf.*, Snowmass, Colorado, 24–28 June (1984).
35. M. A. Merrigan, E. S. Keddy and J. T. Sena, Transient performance investigation of a space power system heat pipe. In *Proc. AIAA/ASME 4th Joint Thermophysics and Heat Transfer Conf.*, AIAA-86-1273, Boston, Massachusetts, 2–4 June (1986).
36. R. E. Cunningham and R. J. J. Williams, *Diffusion in Gases and Porous Media*, Plenum Press, New York (1980).
37. J. G. Collier, *Convective Boiling and Condensation*, pp. 316–328. McGraw-Hill, New York (1981).
38. R. W. Schrage, *A Theoretical Study of Interphase Mass Transfer*. Columbia University Press, New York (1953).
39. S. Hsieh, Metal vapor condensation under high pressure. Ph.D. Thesis, Columbia University (1975).
40. G. A. Somorjai, The evaporation rate and mechanism of CdS and CdSe. In *Proc. Int. Symp. on Condensation and Evaporation of Solids*, Dayton, Ohio, 12–14 September, pp. 417–433 (1962).
41. E. S. Keddy, Personal communication, Los Alamos Laboratory, Los Alamos, New Mexico, 17 December (1986).
42. R. S. Reid, Letter to Michael L. Hall, Los Alamos Laboratory, Los Alamos, New Mexico, 11 February (1987).
43. V. H. Ransom, Personal communication, North Carolina State University, Raleigh, North Carolina, 25 March (1988).

## UNE ETUDE DE SENSIBILITE DES EFFETS DES COEFFICIENTS D'ACCOMMODATION EVAPORATION/CONDENSATION SUR LA MODELISATION EN TRANSITION DES CALODUCS

**Résumé**—Le comportement dynamique des modèles de caloducs à métal liquide est fortement influencé par le choix des techniques de modélisation de l'évaporation et de la condensation. Les descriptions de la théorie cinétique classique de l'évaporation et de la condensation sont souvent inadéquates pour les situations réelles; on utilise communément des coefficients d'accommodation empiriques pour traduire le transfert de masse. Les géométries complexes et les champs d'écoulement dans les systèmes proposés de caloduc causent une déviation importante par rapport aux modèles classiques. Le code THROHPUT qui a été décrit dans des travaux antérieurs, est développé pour modéliser le comportement variable d'un caloduc à métal liquide à partir des conditions de départ jusqu'au fonctionnement permanent de pleine puissance. Ce code est utilisée ici pour évaluer la sensibilité des modèles au choix des coefficients d'accommodation évaporation/condensation. Des comparaisons sont faites avec des résultats expérimentaux. On trouve que le comportement du caloduc peut être prédit avec un choix convenable des coefficients d'accommodation. Néanmoins, l'hypothèse commune de coefficients d'accommodation spatialement constants est un facteur limitant dans le modèle.

## UNTERSUCHUNG DER EMPFINDLICHKEIT EINES TRANSIENTEN WÄRMEROHR-MODELLS AUF EINFLÜSSE DER ANPASSUNGS-KOEFFIZIENTEN FÜR VERDAMPFUNG UND KONDENSATION

**Zusammenfassung**—Das dynamische Verhalten eines Modells für Flüssigmetall-Wärmerohre wird stark davon beeinflußt, wie die Vorgänge der Verdampfung und Kondensation beschrieben werden. Die klassische kinetische Theorie der Verdampfungs- und Kondensationsvorgänge ist für die Beschreibung realer Vorgänge oft ungeeignet; empirische Anpassungs-Koeffizienten werden häufig zur Berücksichtigung des nicht-idealen Stofftransports verwendet. Die komplizierten geometrischen und Strömungsbedingungen, die man von Wärmerohren her kennt, führen zu erheblichen Abweichungen von klassischen Modellen. Das "THROHPUT"-Rechenprogramm, das in früheren Arbeiten vorgestellt worden ist, wurde entwickelt, um das transiente Verhalten von Flüssigmetall-Wärmerohren zu beschreiben, ausgehend von den Startbedingungen mit erstarrtem Metall bis hin zum stationären Betrieb mit voller Leistung. Dieses Programm wird hier dazu verwendet, die Empfindlichkeit des transienten Wärmerohr-Modells für Flüssigmetall auf die Wahl der Anpassungs-Koeffizienten für Verdampfung und Kondensation zu beschreiben. Die Ergebnisse werden mit entsprechenden Versuchsdaten verglichen. Dabei ergibt sich, daß das Verhalten bei richtiger Wahl der Anpassungs-Koeffizienten gut wiedergegeben werden kann. Allerdings stellt die übliche Annahme räumlich konstanter Koeffizienten eine Begrenzung für das Modell dar.

## ИССЛЕДОВАНИЕ ВЛИЯНИЯ АККОМОДАЦИОННЫХ КОЭФФИЦИЕНТОВ ИСПАРЕНИЯ/КОНДЕНСАЦИИ НА МОДЕЛИРОВАНИЕ НЕСТАЦИОНАРНОЙ ТЕПЛОВОЙ ТРУБЫ

**Аннотация**—Динамические характеристики моделей жидкометаллической тепловой трубы сильно зависят от способа описания испарения и конденсации. Классическое описание процессов испарения и конденсации с помощью кинетической теории неадекватно реальной ситуации; эмпирические коэффициенты аккомодации обычно используются для уточнения расчета переноса массы. В случае сложных геометрий и полей течения, характерных для рассматриваемых систем тепловых труб, происходит существенное отклонение от классических моделей. Для исследования функционирования нестационарной жидкометаллической тепловой трубы в диапазоне режимов от начального (запуска) до установившегося составлена программа "THROHPUT", описание которой дано в ранее опубликованных работах. В настоящем исследовании эта программа используется для оценки влияния выбора аккомодационных коэффициентов испарения и конденсации на адекватность моделей нестационарной жидкометаллической тепловой трубы. Проведено сравнение с экспериментальными данными для жидкометаллической тепловой трубы. Найдено, что характеристики тепловой трубы можно достаточно точно рассчитать в случае правильного подбора коэффициентов аккомодации. Показано, что ограничивающим фактором в принятой модели является широко используемое допущение о постоянстве коэффициентов аккомодации в пространстве.